TELKOMNIKA Indonesian Journal of Electrical Engineering
Vol. 12, No. 10, October 2014, pp. 7131 ~ 7142
DOI: 10.11591/telkomnika.v12i8.5328

Strength Analysis for Surface-mounted Permanent Magnet Rotor in High-Speed Motor

Liang-liang Chen*, Chang-sheng Zhu
Zhejiang University,
38 Zheda Road, Hangzhou 310027, China; telp: 0086-0571-87983515
*Corresponding author, e-mail: chenlian0510@163.com

Abstract

In the surface-mounted high-speed permanent magnet motor, the magnets are not mechanically strong enough to bear the centrifugal stress resulted from the high speed rotating, thus a sleeve composed of the carbon-fiber bandage is usually employed to retain the permanent magnets on the rotor surface. According to the surface-mounted high-speed permanent magnet rotor retained by a carbon-fiber bandage, in this paper, an analytical model for calculating rotor strength was presented based on the theory of elastic mechanics. Then the results of analytical model were compared with the calculations of finite-element method. It was shown that the analytical model proposed in this paper could accurately predict the stress distribution of the surface-mounted high-speed permanent magnet rotor fixed by a carbon-fiber bandage. Finally, the influence of the bandage thickness and shrink range between the permanent magnets and the bandage on rotor stress was investigated based on this analytical model of rotor strength.

Keywords*: carbon-fiber bandage, high-speed, permanent magnet motor, strength analysis*

1. Introduction

Nowadays, surface-mounted high speed permanent magnet (PM) motor is becoming more and more common due to its simple structure, high power density and increased efficiency [1, 2]. In the surface-mounted high speed PM motor, the magnets generally consist of separate blocks which are glued onto the rotor surface. Several kinds of permanent magnetic materials, such as alnico magnets, ferrite magnets and rare-earth magnets, are usually employed in the high speed PM motor. Among them, the rare-earth magnets are widely applied owing to its high saturation intensity and coercive force [3]. However, this kind of PM material has high compressive strength but low tensile strength, and can not sustain the centrifugal stress due to high speed rotation. Therefore, it must be contained in a sleeve. Generally, there are two kinds of sleeves, one is nonmagnetic alloy sleeve such as titanium alloy, the other is high-strength composite materials such as carbon-fiber bandages. The carbon-fiber bandage has a high strength to weight ratio and low eddy-current losses compared to the alloy sleeve [4, 5]. So carbon-fiber bandage is more often employed as the retaining sleeve in the high-speed PM motor [6-9]. The centrifugal stress of PMs can be compensated by pre-stress applied to the outer surface of PMs through magnet-sleeve interference fit. In order to determine the pre-stress, shrink range and sleeve thickness, the rotor strength must be analyzed firstly. So rotor strength analysis is a key point in the rotor design of the surface-mounted high speed PM motor.

There have been some papers discussing the mechanical strength of the high speed PM rotor contained in a sleeve. Finite-element method (FEM) was usually applied to rotor strength analysis [10, 11]. Analytical strength model for the cylindrical PM rotor retained by a nonmagnetic alloy sleeve were presented in [12-14]. A simple calculation strategy for the cylindrical PM rotor retained by a carbon-fiber bandage was presented in [15], but the effect of anisotropy of the carbon-fiber on rotor stress was not considered in the analytical model. At present, the rotor strength of the surface-mounted high speed PM motor is mainly analyzed by FEM. However, FEM is time-consuming, and may lead to no convergence. The analytical method for rotor strength mainly focuses on the cylindrical PM rotor retained by a nonmagnetic alloy sleeve. Nevertheless, the stress distribution for the surface-mounted PM rotor retained by a carbon-fiber bandage is different from that of the cylindrical PM rotor retained by a

Received December 9, 2013; Revised June 15, 2014; Accepted July 10, 2014

nonmagnetic alloy sleeve due to the centrifugal forces of separate PM blocks and the effect of anisotropy of carbon-fiber bandage. Therefore, the analytical method for the surface-mounted PM rotor retained by a carbon-fiber bandage needs further study. In this investigation for the surface-mounted PM rotor with a carbon-fiber bandage, the analytical model for calculating rotor strength is deduced based on the rotor stress condition which is simplified as a plane stress problem. The analytical solutions are validated by corresponding finite element results. The comparison results demonstrate that the analytical model presented in this paper can accurately predict the radial stress, tangential stress and equivalent Von-Mises stress of the surface-mounted high speed PM rotor fixed by a carbon-fiber bandage. Subsequently, the impact of the bandage thickness and shrink range between the PMs and bandage on rotor stress is discussed based on this analytical model of rotor strength.

2. Rotor Structure of the Surface-mounted High Speed PM Motor

The construction of the surface-mounted high speed PM rotor for this investigation is shown in Figure 1. The permanent magnets are glued onto the rotor surface and fixed by a carbon-fiber bandage. To achieve a defined pre-stress and a defined contact force, the bandage is designed as prefabricated sleeve made from carbon-fiber, which is embedded within an epoxy resin matrix.

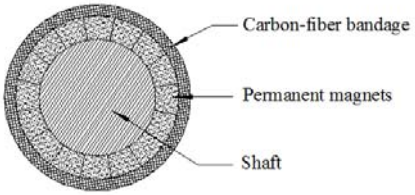

Figure 1. The Rotor Structure of the Surface-mounted High Speed PM Motor

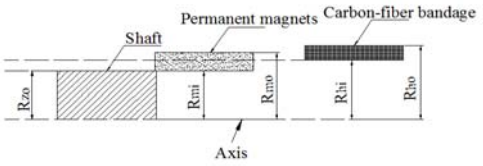

Figure 2. The Dimensions of the Surface-mounted High Speed PM Rotor

The dimensions of the rotor are shown in Figure 2. R_{zo} is the outer radius of the shaft, R_{mi} and R_{mo} are the inner radius and outer radius of the PMs, respectively. Similarly, R_{hi} and R_{ho} are the inner radius and outer radius of the carbon-fiber bandage. There is a shrink range between the PMs and the carbon-fiber bandage, the outer radius of the shaft is equal to the inner radius of PMs, i.e.

$$\begin{cases} R_{zo} - R_{mi} = 0 \\ R_{mo} - R_{hi} = \delta \end{cases} \quad (1)$$

Where δ is the shrink range.

3. Analytical Model for Rotor Strength in the Surface-Mounted High Speed PM Motor

In order to simplify theoretical analysis, the following assumptions are made: a) all permanent magnet blocks have the same properties; b) there is no gap between PMs, i.e., the pole coverage ratio is 100%; c) the rotor stress condition is simplified as a plane stress problem.

3.1. Analytical Model for Contact Pressures Between the PMs and Other Rotor Parts

In this paper, it is assumed that P_1 is the contact pressure between the PMs and the shaft, and P_2 is the contact pressure between the PMs and carbon-fiber bandage.

3.1.1. Radial Displacement in the Inner Surface of the Carbon-fiber Bandage

The carbon-fiber bandage is considered as the orthotropic materials in this section. Figure 3 shows the force diagram of the carbon-fiber bandage. As can be seen in figure 3, the compressive stress P_2 acts on the inner surface of the bandage.

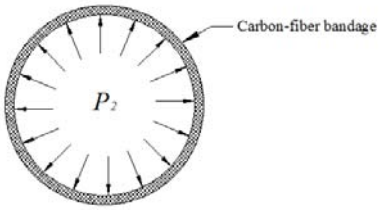

Figure 3. The Force Diagram of the Carbon-fiber Bandage

According to the theory of elastic mechanics, the equilibrium differential equation of the carbon-fiber bandage is:

$$\frac{d\sigma_r}{dr}+\frac{\sigma_r\text{-}\sigma_\theta}{r}+\rho_h r\omega^2=0 \tag{2}$$

Where σ_r and σ_θ are the radial stress and tangential stress of the carbon-fiber bandage in the radius of *r*, respectively. ρ_h is the density of the carbon-fiber bandage, and ω is the angular velocity.

The physical relations of the carbon-fiber bandage are:

$$\varepsilon_r=\frac{\sigma_r}{E_r}-\frac{\mu_{\theta r}}{E_\theta}\sigma_\theta,\varepsilon_\theta=\frac{\sigma_\theta}{E_\theta}-\frac{\mu_{r\theta}}{E_r}\sigma_r \tag{3}$$

Where ε_r and ε_θ are radial strain and tangential strain of the carbon-fiber bandage, respectively. E_r and E_θ are radial young's modulus and tangential Young's modulus of the carbon-fiber bandage, respectively, while $\mu_{\theta r}$ and $\mu_{r\theta}$ are major and minor Poisson's ratio.

The geometric relations of the carbon-fiber bandage are:

$$\varepsilon_\theta=\frac{u_r}{r},\varepsilon_r=\frac{du_r}{dr} \tag{4}$$

Where u_r is the radial displacement of the carbon-fiber bandage in the radius of *r*.

The combination of differential Equation (2) with Equation (3) and (4) yields:

$$r^2\frac{d^2\sigma_r}{dr^2}+3r\frac{d\sigma_r}{dr}+(1-k^2)\sigma_r=-(3+\mu_{\theta r})\rho_h\omega^2r^2 \tag{5}$$

Where $k=\sqrt{E_\theta/E_r}$.

Solving differential Equation (5), we obtained:

$$\sigma_r=c_1r^{k-1}+c_2r^{-k-1}+\frac{\rho_h\omega^2r^2(3+\mu_{\theta r})}{k^2-9} \tag{6}$$

Where c_1 and c_2 are undetermined coefficients.

The boundary Conditions of the carbon-fiber bandage are:

$$\sigma_r\Big|_{r=R_{ho}}=0,\sigma_r\Big|_{r=R_{hi}}=-p_2 \tag{7}$$

Introducing Equation (7) into Equation (6), the coefficients c_1 and c_2 can be obtained:

$$\begin{cases} c_1 = \dfrac{-P_2}{R_{ho}^{k-1}(\alpha^{k-1}-\alpha^{-k-1})} - \dfrac{\rho_h\omega^2 R_{ho}^2(3+\mu_{\theta r})(1-\alpha^{3+k})}{R_{ho}^{k-1}(k^2-9)(1-\alpha^{2k})} \\ c_2 = \dfrac{-P_2}{R_{ho}^{-k-1}(\alpha^{-k-1}-\alpha^{k-1})} - \dfrac{\rho_h\omega^2 R_{ho}^2(3+\mu_{\theta r})(1-\alpha^{3-k})}{R_{ho}^{-k-1}(k^2-9)(1-\alpha^{-2k})} \end{cases} \quad (8)$$

The combination of differential equation (2) with equation (6) yields:

$$\sigma_\theta = kc_1 r^{k-1} - kc_2 r^{-k-1} + \frac{3\rho_h\omega^2 r^2(3+\mu_{\theta r})}{k^2-9} + \rho_h\omega^2 r^2 \quad (9)$$

From equations (3) and (4), we can obtain:

$$u_r = r\left(\frac{\sigma_\theta}{E_\theta} - \frac{\mu_{r\theta}\sigma_r}{E_r}\right) \quad (10)$$

Substituting equations (6) and (9) into equation (10) yields:

$$u_r = \left(\frac{k}{E_\theta} - \frac{\mu_{r\theta}}{E_r}\right) c_1 r^k + \left(\frac{-k}{E_\theta} - \frac{\mu_{r\theta}}{E_r}\right) c_2 r^{-k} + \left(\frac{3}{E_\theta} - \frac{\mu_{r\theta}}{E_r}\right)\frac{\rho_h\omega^2(3+\mu_{\theta r})r^3}{k^2-9} + \frac{\rho_h\omega^2 r^3}{E_\theta} \quad (11)$$

Let $r=R_{hi}$ in equation (11), the radial displacement in the inner surface of the carbon-fiber bandage is obtained:

$$u_{hi} = \left(\frac{k}{E_\theta} - \frac{\mu_{r\theta}}{E_r}\right) c_1 R_{hi}^k + \left(\frac{-k}{E_\theta} - \frac{\mu_{r\theta}}{E_r}\right) c_2 R_{hi}^{-k} + \left(\frac{3}{E_\theta} - \frac{\mu_{r\theta}}{E_r}\right)\frac{\rho_h\omega^2(3+\mu_{\theta r})R_{hi}^3}{k^2-9} + \frac{\rho_h\omega^2 R_{hi}^3}{E_\theta} \quad (12)$$

3.1.2. Radial Displacements in the Inner and Outer Surfaces of PMs

The PMs are considered as the isotropic materials in this section. The force diagram of the PMs is shown in Figure 4. The compressive stress P_2 acts on the outer surface, while P_1 acts on the inner surface. As the PMs are segmented, the centrifugal forces of the PM blocks act on the inner surface of the carbon-fiber bandage directly. Consequently, P_2 is decomposed into the centrifugal pressure P_{2w}, which is produced by the centrifugal forces of the PM blocks, and the shrinking pressure (P_2-P_{2w}) generated by magnet-sleeve interference fit. Similarly, P_1 is decomposed into the centrifugal pressure P_{1w}, and the shrinking pressure (P_1-P_{1w}).

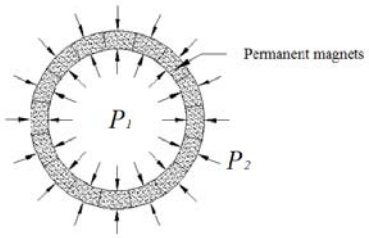

Figure 4. The force diagram of segmented PMs

With the action of shrinking pressure (P_1-P_{1w}) and (P_2-P_{2w}), the radial displacement in the inner surface of PMs [16] is:

$$u_{mip} = \frac{(P_1 - P_{2w})\ R_{mi}}{E_m}(\mu_m + \frac{R_{mo}^2 + R_{mi}^2}{R_{mo}^2 - R_{mi}^2}) - \frac{2(P_2 - P_{2w})R_{mi}R_{mo}^2}{E_m(R_{mo}^2 - R_{mi}^2)} \quad (13)$$

where E_m and μ_m are Young's modulus and Poisson's ratio of the PMs, respectively.

The radial displacement in the outer surface of PMs is

$$u_{mop} = \frac{2(P_1 - P_{1w})R_{mi}^2 R_{mo}}{E_m(R_{mo}^2 - R_{mi}^2)} + \frac{(P_2 - P_{2w})R_{mo}}{E_m}(\mu_m - \frac{R_{mo}^2 + R_{mi}^2}{R_{mo}^2 - R_{mi}^2}) \quad (14)$$

The centrifugal force of a PM block in the radius of r is

$$F_w(r) = \rho_m \frac{\pi(r^2 - R_{mi}^2)L\omega^2}{N} \cdot \frac{(r + R_{mi})}{2} \quad (15)$$

where ρ_m is the density of the PMs, N is the number of PM blocks, L is the axial length. If the force F_w is evenly distributed along the circumference of the PM, the centrifugal pressure P_w in the radius of r is obtained:

$$P_w = \frac{NF_w}{2\pi rL} = \frac{\rho_m \omega^2 (r^2 - R_{mi}^2)(r + R_{mi})}{4r} \quad (16)$$

Let $r=R_{mi}$ and $r=R_{mo}$ in equation (16), respectively, P_{1w} and P_{2w} can be obtained:

$$\begin{cases} P_{1w} = 0 \\ P_{2w} = \dfrac{NF_w}{2\pi R_{mo}L} = \dfrac{\rho_m(R_{mo}^2 - R_{mi}^2)\omega^2(R_{mo} + R_{mi})}{4R_{mo}} \end{cases} \quad (17)$$

Neglecting the interactive force between PMs, the deformation of PMs in the radius of r, generated by the centrifugal force, is

$$\Delta(r) = \int_{R_{mi}}^{r} \frac{P_w}{E_m} dr = \frac{\rho_m \omega^2}{4E_m}(\frac{r^3}{3} + \frac{R_{mi}r^2}{2} - R_{mi}^2 r - R_{mi}^3 \ln r + \frac{R_{mi}^3}{6} + R_{mi}^3 \ln(R_{mi})) \quad (18)$$

Generally, tensile direction is regarded as the positive direction in the elastic theory, so the radial displacement of the PM, resulted from the centrifugal force, is

$$u_{m\omega}(r) = -\Delta(r) = -\frac{\rho_m \omega^2}{4E_m}(\frac{r^3}{3} + \frac{R_{mi}r^2}{2} - R_{mi}^2 r - R_{mi}^3 \ln r + \frac{R_{mi}^3}{6} + R_{mi}^3 \ln(R_{mi})) \quad (19)$$

Let $r=R_{mi}$ and $r=R_{mo}$ in equation (19), respectively, the radial displacement in the inner surface and outer surface of the PMs, resulted from centrifugal force, can be obtained:

$$\begin{cases} u_{mi\omega} = 0 \\ u_{mo\omega} = -\dfrac{\rho_m \omega^2}{4E_m}(\dfrac{R_{mo}^3}{3} + \dfrac{R_{mi}R_{mo}^2}{2} - R_{mi}^2 R_{mo} - R_{mi}^3 \ln(R_{mo}) + \dfrac{R_{mi}^3}{6} + R_{mi}^3 \ln(R_{mi})) \end{cases} \quad (20)$$

Considering the pre-pressure and centrifugal force of thePMs, the total radial displacement in the inner surface of PMs is:

$$u_{mi} = u_{mip} + u_{mi\omega} = \frac{P_1 R_{mi}}{E_m}(\mu_m + \frac{R_{mo}^2 + R_{mi}^2}{R_{mo}^2 - R_{mi}^2}) - \frac{2(P_2 - P_{2w})R_{mi}R_{mo}^2}{E_m(R_{mo}^2 - R_{mi}^2)} \quad (21)$$

The total radial displacement in the outer surface of PMs is:

$$u_{mo}=u_{mop}+u_{mo\omega}=\frac{2P_1R_{mi}^2R_{mo}}{E_m(R_{mo}^2-R_{mi}^2)}+\frac{(P_2-P_{2w})R_{mo}}{E_m}(\mu_m-\frac{R_{mo}^2+R_{mi}^2}{R_{mo}^2-R_{mi}^2})$$
$$-\frac{\rho_m\omega^2}{4E_m}(\frac{R_{mo}^3}{3}+\frac{R_{mi}R_{mo}^2}{2}-R_{mi}^2R_{mo}-R_{mi}^3\ln(R_{mo})+\frac{R_{mi}^3}{6}+R_{mi}^3\ln(R_{mi})) \quad (22)$$

3.1.3. Radial Displacement in the Outer Surface of the Shaft

The shaft is also considered as the isotropic materials in this secton. Figure 5 shows the force diagram of the shaft. There is a compressive stress P_1 in the outer surface of the shaft. Under the action of contact pressure P_1 and centrifugal force of the shaft, the radial displacement in the outer surface of the shaft [16] is:

$$u_{zo}=-\frac{P_1R_{zo}}{E_z}(1-\mu_z)+\frac{1}{4}\cdot\frac{\rho_z\omega^2R_{zo}^3}{E_z}(1-\mu_z) \quad (23)$$

Where E_z and μ_z are Young's modulus and Poisson's ratio of the shaft, respectively.

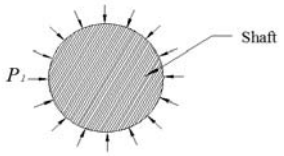

Figure 5. The Force Diagram of the Shaft

3.1.4. Solutions of P_1 and P_2

According to the boundary conditions of the PM rotor, the following equation is obtained:

$$\begin{cases}u_{mi}-u_{zo}=0\\u_{hi}-u_{mo}=\delta\end{cases} \quad (24)$$

Substituting Equation (12), (21), (22) and (23) into Equation (24), P_1 and P_2 can be obtained:

$$\begin{cases}P_1=\dfrac{K_{22}\delta_1-K_{12}\delta_2}{K_{11}K_{22}-K_{12}K_{21}}\\P_2=\dfrac{\delta_2-K_{21}P_1}{K_{22}}\end{cases} \quad (25)$$

Where,

$$K_{11}=\frac{R_{mi}}{E_m}(\mu_m+\frac{R_{mo}^2+R_{mi}^2}{R_{mo}^2-R_{mi}^2})+\frac{R_{zo}}{E_z}(1-\mu_z),\quad K_{12}=-\frac{2R_{mi}R_{mo}^2}{E_m(R_{mo}^2-R_{mi}^2)},\quad K_{21}=-\frac{2R_{mi}^2R_{mo}}{E_m(R_{mo}^2-R_{mi}^2)},$$
$$K_{22}=\frac{-R_{hi}^k}{R_{ho}^{k-1}(\alpha^{k-1}-\alpha^{-k-1})}(\frac{k}{E_\theta}-\frac{\mu_{r\theta}}{E_r})-\frac{R_{hi}^{-k}}{R_{ho}^{-k-1}(\alpha^{-k-1}-\alpha^{k-1})}(\frac{-k}{E_\theta}-\frac{\mu_{r\theta}}{E_r})-\frac{R_{mo}}{E_m}(\mu_m-\frac{R_{mo}^2+R_{mi}^2}{R_{mo}^2-R_{mi}^2}),$$
$$\delta_1=\frac{1}{4}\cdot\frac{\rho_z\omega^2R_{zo}^3}{E_z}(1-\mu_z)-\frac{2P_{2w}R_{mi}R_{mo}^2}{E_m(R_{mo}^2-R_{mi}^2)},$$

$$\delta_2=\delta+\frac{\rho_h\omega^2R_{ho}^2R_{hi}^k(3+\mu_{\theta r})(1-\alpha^{3+k})}{R_{ho}^{k-1}(k^2-9)(1-\alpha^{2k})}(\frac{k}{E_\theta}-\frac{\mu_{r\theta}}{E_r})+\frac{\rho_h\omega^2R_{ho}^2R_{hi}^{-k}(3+\mu_{\theta r})(1-\alpha^{3-k})}{R_{ho}^{k-1}(k^2-9)(1-\alpha^{-2k})}(\frac{-k}{E_\theta}-\frac{\mu_{r\theta}}{E_r})-\frac{\rho_h\omega^2R_{hi}^3(3+\mu_{\theta r})}{k^2-9}(\frac{3}{E_\theta}-\frac{\mu_{r\theta}}{E_r})$$
$$-\frac{\rho_h\omega^2R_{hi}^3}{E_\theta}-\frac{\rho_m\omega^2}{4E_m}(\frac{R_{mo}^3}{3}+\frac{R_{mi}R_{mo}^2}{2}-R_{mi}^2R_{mo}-R_{mi}^3\ln(R_{mo})+\frac{R_{mi}^3}{6}+R_{mi}^3\ln(R_{mi}))-\frac{P_{2w}R_{mo}}{E_m}(\mu_m-\frac{R_{mo}^2+R_{mi}^2}{R_{mo}^2-R_{mi}^2})$$

3.2. Stress Model for the Surface-mounted High Speed PM Rotor

After obtaining the contact pressures P_1 and P_2, the stresses in the carbon-fiber bandage and PMs can be deduced based on the theory of elastic mechanics.

3.2.1. Stress Model for the Carbon-fiber Bandage

The radial stress of the carbon-fiber bandage can be calculated by Equation (6) and (8), while the tangential stress is computed by Equation (8) and (9).

The equivalent Von-Mises stress of the carbon-fiber bandage is:

$$\sigma_{hMises}=\sqrt{\frac{1}{2}[(\sigma_r-\sigma_\theta)^2+(\sigma_r)^2+(\sigma_\theta)^2]} \tag{26}$$

3.2.2. Stress Model for the PMs

The shrinking radial stress of the PMs is expressed as:

$$\sigma_{rm}=\frac{(P_1R_{mi}^2-P_2R_{mo}^2)}{R_{mo}^2-R_{mi}^2}-\frac{R_{mi}^2R_{mo}^2(P_1-P_2)}{(R_{mo}^2-R_{mi}^2)r^2}+P_{2w}\frac{R_{mo}^2}{R_{mo}^2-R_{mi}^2}(1-\frac{R_{mi}^2}{r^2}) \tag{27}$$

The shrinking tangential stress is:

$$\sigma_{\theta m}=\frac{(P_1R_{mi}^2-P_2R_{mo}^2)}{R_{mo}^2-R_{mi}^2}+\frac{R_{mi}^2R_{mo}^2(P_1-P_2)}{(R_{mo}^2-R_{mi}^2)r^2}+P_{2w}\frac{R_{mo}^2}{R_{mo}^2-R_{mi}^2}(1+\frac{R_{mi}^2}{r^2}) \tag{28}$$

The centrifugal radial stress is:

$$\sigma_{rm\omega}=\frac{E_m}{1-\mu_m^2}(\frac{du_{m\omega}}{dr}+\mu_m\frac{u_{m\omega}}{r})=-\frac{\rho_m\omega^2}{4(1-\mu_m^2)}[r^2+R_{mi}r-R_{mi}^2-\frac{R_{mi}^3}{r}+\mu_m(\frac{r^2}{3}+\frac{R_{mi}r}{2}-R_{mi}^2-\frac{R_{mi}^3}{r}\ln r+\frac{R_{mi}^3}{6r}+\frac{R_{mi}^3}{r}\ln R_{mi})] \tag{29}$$

The centrifugal tantengial stress is:

$$\sigma_{\theta m\omega}=\frac{E_m}{1-\mu_m^2}(\frac{u_{m\omega}}{r}+\mu_m\frac{du_{m\omega}}{dr})=-\frac{\rho_m\omega^2}{4(1-\mu_m^2)}[\frac{r^2}{3}+\frac{R_{mi}r}{2}-R_{mi}^2-\frac{R_{mi}^3}{r}\ln r+\frac{R_{mi}^3}{6r}+\frac{R_{mi}^3}{r}\ln(R_{mi})+\mu_m(r^2+R_{mi}r-R_{mi}^2-\frac{R_{mi}^3}{r})] \tag{30}$$

The total radial stress of PMs is:

$$\sigma_{rm}^d=\sigma_{rm}+\sigma_{rm\omega} \tag{31}$$

The total tantengial stress of PMs is:

$$\sigma_{\theta m}^d=\sigma_{\theta m}+\sigma_{\theta m\omega} \tag{32}$$

The total equivalent Von-Mises stress of the PMs can be calculated as:

$$\sigma_{mMises}^d=\sqrt{\frac{1}{2}[(\sigma_{rm}^d-\sigma_{\theta m}^d)^2+(\sigma_{rm}^d)^2+(\sigma_{\theta m}^d)^2]} \tag{33}$$

4. Comparison of the Analytical Model and Finite Element Results

In order to validate the analytical model for rotor strength, the stress distribution of a surface-mounted high speed PM rotor retained by a carbon-fiber bandage is analyzed by the analytical model presented in this paper and FEM, respectively. In FEM, a two-dimensional model was used to analyze the stress of the rotor, and the average stress along the circumference is compared with the analytical results. The rated speed of the motor is 24000 *rpm*, the number of PM blocks is 4, and the shrink range between the PMs and carbon-fiber bandage is 0.1 *mm*. Table 1 shows the basic parameters of the PM rotor.

Table 1. The Basic Parameters of the PM Rotor

	Shaft	PM	Carbon-fiber bandage
Inner radius (*mm*)	0	43	50
Outer radius (*mm*)	43	50	54
Density (kg/m^3)	7850	8300	1750
Radial Young's modulus (P_a)	2.1×10^{11}	1.08×10^{11}	2.7×10^{10}
Tangential Young's modulus(P_a)	2.1×10^{11}	1.08×10^{11}	4.56×10^{11}
Poisson's ratio	μ_z =0.31	μ_m =0.24	$\mu_{\theta r}$=0.3, $\mu_{r\theta}$=0.018

4.1. The Stress Distribution of the PMs and Carbon-fiber Bandage without Rotational Speed

In case of no rotation, the stresses of PMs along the radius direction are shown in Figure 6~Figure 8, while the stresses of the carbon-fiber bandage are shown in Figure 9~Figure 11. In the figures, the stars represent the calculations of FEM, while the solid line stands for calculations of the analytical model. The dotted line represents the error between the results calculated by two different methods. The negative value indicates that the stress is a compressive stress.

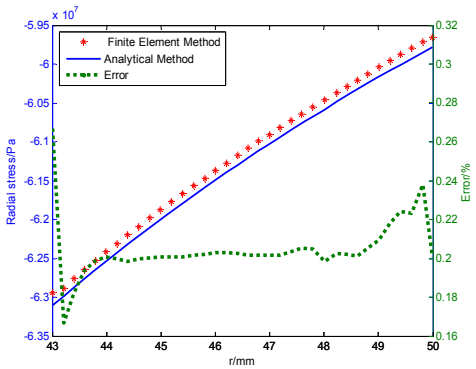

Figure 6. The Radial Stress of PMs along the Radius Direction

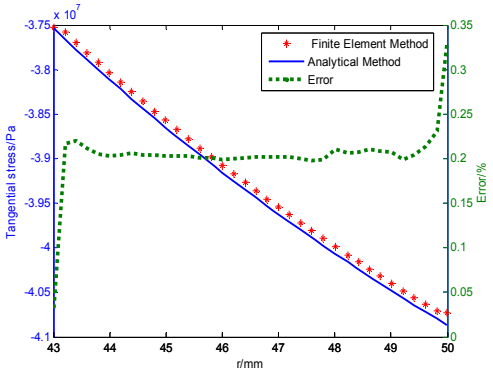

Figure 7. The Tangential Stress of PMs along the Radius Direction

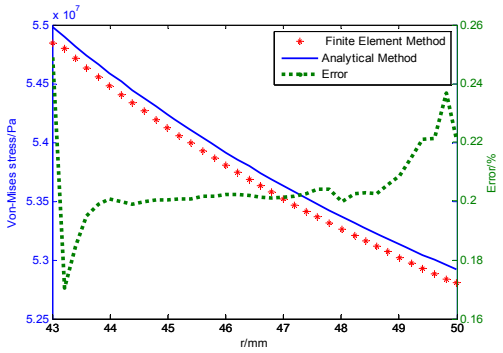

Figure 8. The Equivalent Von-Mises Stress of PMs along the Radius Direction

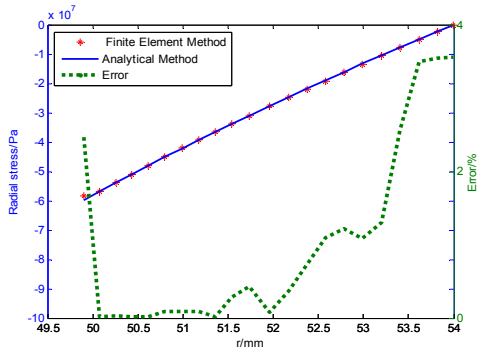

Figure 9. The Radial Stress of Carbon-fiber Bandage along the Radius Direction

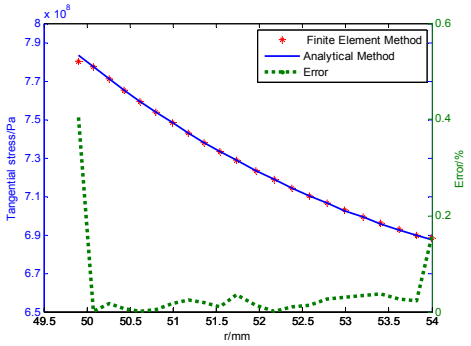

Figure 10. The Tangential Stress of Carbon-fiber Bandage along the Radius Direction

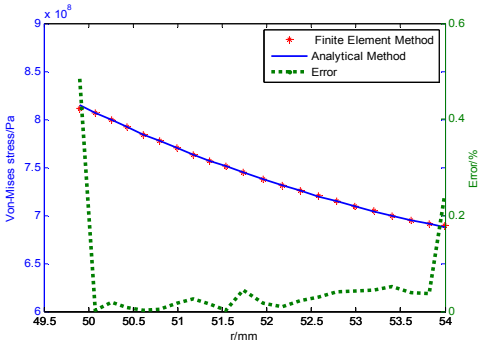

Figure 11. The Equivalent Von-Mises Stress of Carbon-fiber Bandage along the Radius Direction

As can be seen from these figures, the calculation results of the analytical model are close to finite-element calculations, and the maximum error is less than 4%. The radial stress and equivalent Von-Mises stress of the PMs both decrease with the increase of radius, while the tangential stress increases with the radius. The maximum equivalent Von-Mises stress of PMs occurs at the inner surface. In Engineering, the maximum equivalent Von-Mises stress should not exceed the compressive strength of the PMs. From Figure 8, We can learn that the maximum equivalent Von-Mises stress is about 55 Mp_a, which is much less than the compressive strength of PMs (about 600Mp_a). The radial stress, tangential stress and equivalent Von-Mises stress of the carbon-fiber bandage all decrease along the radius direction. The maximum equivalent Von-Mises stress of the carbon-fiber bandage also occurs at the inner surface. The carbon-fiber bandage is orthotropic materials. So it must be ensured that the maximum radial stress and tangential stress of the carbon-fiber bandage do not exceed the radial tensile strength and tangential tensile strength, respectively. In this section, the maximum radial stress of the carbon-fiber bandage is about 60 MP_a, which is much less than the radial tensile strength (about 400 MP_a), on the other hand, the maximum tangential stress (about 790 MP_a) is also less than the tangential tensile strength (about 2600 MP_a).

4.2. The Stress Distribution of the PMs and Carbon-fiber Bandage at the Speed of 24000 rpm

At the rated speed, the stresses of PMs are shown in Figure 12～Figure 14, and the stresses of carbon-fiber bandage are shown in Figure 15～Figure 17. The results demonstrate that the stresses calculated by two methods are also in good agreement with each other, and the maximum error is less than 3.5%. Compared with no rotation case, here the radial stress of PMs becomes less, and the radial stress increases along the radius direction, which is opposite to that in no rotation case. Besides, the tangential stress and equivalent Von-Mises stress of the PMs also become less owing to the effect of centrifugal force. In the design of surface-mounted high speed PM rotor, it must be ensure that the PMs are in compression at the rated speed, i.e., the radial stress and tangential stess should be less than zero. The maximum equivalent Von-Mises stress of the PMs transfers from the inner surface to the outer surface due to the effect of centrifugal force, and it is also less than the compressive strength of PMs. The radial stress, tangential stress and equivalent Von-Mises stress of the carbon-fiber bandage become larger due to the effect of the centrifugal force. At high speed case, the maximum Von-Mises stress of the carbon-fiber bandage also occurs at the inner surface. The maximum radial stress and tangential stress are also less than the radial tensile strength and tangential tensile strength, respectively.

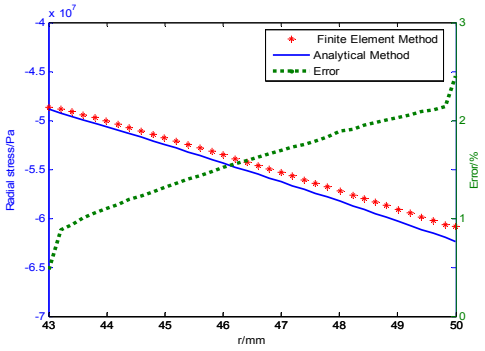

Figure 12. The Radial Stress of PMs along the Radius Direction at the Speed of 24000 rpm

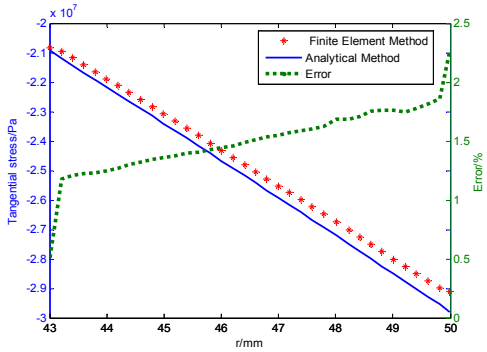

Figure 13. The Tangential Stress of PMs along the Radius Direction at the Speed of 24000 rpm

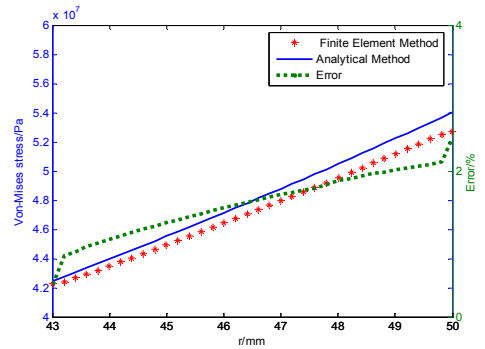

Figure 14. The Equivalent Von-Mises Stress of PMs along the Radius Direction at the Speed of 24000 rpm

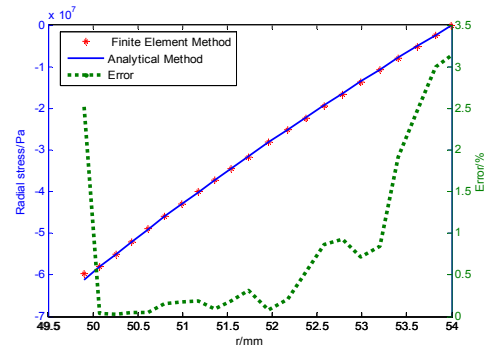

Figure 15. The Radial Stress of Carbon-fiber Bandage along the Radius Direction at the Speed of 24000 rpm

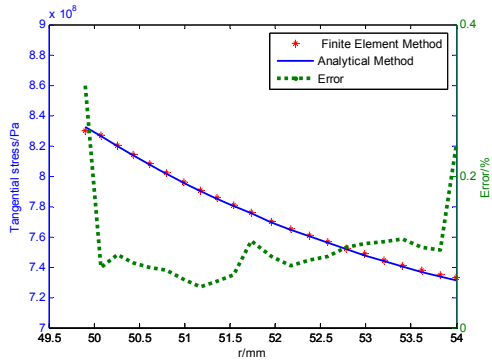

Figure 16. The Tangential Stress of Carbon-Fiber Bandage along the Radius Direction at the Speed of 24000 rpm

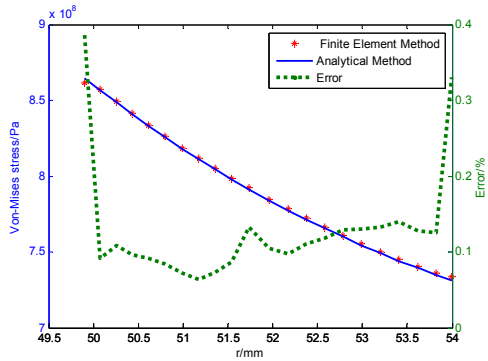

Figure 17. The Equivalent Von-Mises Stress of Carbon-fiber Bandage along the Radius Direction at the Speed of 24000 rpm

5. Discussion for the Rotor Strength

In this section, the impact of the bandage thickness and the shrink range between the PMs and carbon-fiber bandage on rotor stress is investigated based on the analytical model of rotor strength proposed by this paper. The shrink range δ and thickness of the carbon-fiber bandage are taken as the input variables, while the residual contact pressure P_2 and the maximum equivalent Von-Mises stress σ_{max} of the carbon-fiber bandage are regarded as the output variables. Figure 18 shows the relationship between P_2 and input variables at the speed of 24000 *rpm*, while Figure 19 shows the variations of the maximum equivalent Von-Mises stress σ_{max} of the carbon- fiber bandage with the input variables. As can been seen from the two

figures, while the bandage thickness remains a constant, the residual contact pressure P_2 and the maximum equivalent Von-Mises stressσ_{max} increase significantly with the shrink range δ rising up. When the shrink range δ is a constant, P_2 rises fast with the bandage thickness increase, however, the maximum equivalent Von-Mises stress decreases slowly with increasing thickness of the carbon-fiber bandage. Therefore, in the design of the surface-mounted high speed PM motor, the residual contact pressure can be enhanced by means of increasing the shrink range δ or bandage thickness. Because the residual contact pressure P_2 and the maximum equivalent Von-Mises stressσ_{max} both increase fast with increasing δ, in order to ensure the maximum stress of the carbon-fiber bandage is less than the tensile strength, the shrink range δ should be carefully selected.

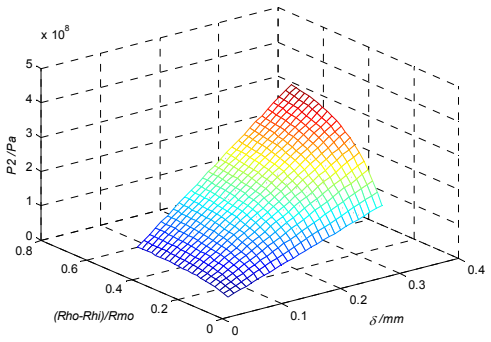

Figure 18. Residual Contact Pressure P_2 at the Speed of 24000 rpm

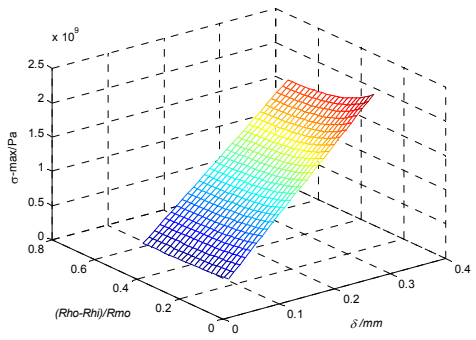

Figure 19. The Maximum Equivalent Von-Mises Stress of the Carbon-fiber Bandage at the Speed of 24000 rpm

6. Conclusion

In this paper, an analytical strength model for the surface-mounted high speed PM rotor retained by a carbon-fiber bandage is presented based on the elastic theory. Then the analytical solutions are compared with the finite-element results. The comparison results show that the results of analytical model match the FEM calculations, and the analytical model presented in this paper can accurately analyze the radial stress, tangential stress and equivalent Von-Mises stress of the surface-mounted high speed PM rotor fixed by a carbon-fiber bandage. Then, based on the analytical model of rotor strength, the influence of the bandage thickness and the shrink range on rotor stress is discussed. According to the results of investigation, the residual contact pressure can be enhanced by increasing the shrink range δ or bandage thickness, and the maximum equivalent Von-Mises stress can be decreased by increasing the bandage thickness. In addition, in order to ensure the maximum stress of the carbon-fiber bandage is less than the tensile strength, the shrink range δ should be carefully selected. The researches in this paper provide theoretical support for design and optimization of the surface-mounted high speed PM motor.

References

[1] Ilka R, Gholamian SA. Optimum Design of a Five-Phase Permanent Magnet Synchronous Motor for Underwater Vehicles by use of Particle Swarm Optimization. *Telkomnika.* 2012; 10(5): 925-932.
[2] Cheng F, Xu HP, Xue SS. *Study on the Design Method of High Speed Permanent Magnet Synchronous Machine.* Proceedings of International Conference on Electrical Machines and Systems. Beijing. 2011:1-6.
[3] Bochenkov B, Lutz S. *A Review of Modern Materials of Permanent Magnets*. Proceedings of the 8th Russian-Korean International Symposium on Science and Technology. Tomsk. 2004: 201-203.
[4] Kolondzovski Z, Arkkio A, Larjola J, Sallinen P. Power Limits of High-Speed Permanent-Magnet Electrical Machines for Compressor Applications. *IEEE Transactions on Energy Conversion*. 2011; 26(1):73-82.

[5] Kolondzovski Z, Belahcen A, Arkkio A. Comparative Thermal Analysis of Different Rotor Types for a High-Speed Permanent-Magnet Electrical Machine. *IET Electric Power Application*. 2009; 3(4): 279-288.
[6] Cho HW, Jang SM, Choi SK. A Design Approach to Reduce Rotor Losses in High-Speed Permanent Magnet Machine for Turbo-Compressor. *IEEE Transactions on Magnetics*. 2006; 42(10): 3521 – 3523.
[7] Kenny BH, Kascak PE, Jansen R, Dever T, Santiago W. Control of a High-Speed Flywheel System for Energy Storage in Space Applications. *IEEE Transactions on Iddustry Applications*. 2005; 41(4): 1029 - 1038.
[8] Aglen O. *Loss Calculation and Thermal Analysis of a High-Speed Generator*. Proceedings of IEEE International Electric Machines and Drives Conference. Chicago. 2010: 1117-1121.
[9] Paulides JJH, Jewell GW, Howe D. An Evaluation of Alternative Stator Lamination Materials for a High-Speed 1.5 MW Permanent Generator. *IEEE Transactions on Magnetics*. 2004; 40(4):2041–2043.
[10] Zhang T, Ye XT, Zhang HP, Jia HY. Strength Design on Permanent Magnet Rotor in High Speed Motor Using Finite Element Method. *Telkomnika*. 2014; 12(3): 1758-1763.
[11] Bailey C, Saban DM, Paulo GP. Design of High-Speed Direct-Connected Permanent-Magnet Motors and Generators for the Petrochemical Industry. *IEEE Transactions on Industry Applications*. 2009; 45(3): 1159-1165.
[12] Borisavljevic A, Polinder H, Ferreira JA. On the Speed Limits of Permanent-Magnet Machines. *IEEE Transtions on Industrial Electronics*. 2010; 57(1): 220-226.
[13] Riemer B, Leßmann M, Hameyer K. *Rotor Design of a High-Speed Permanent Magnet Synchronous Machine rating 100,000 rpm at 10 kW*. Proceedings of IEEE Energy Conversion Congress and Exposition. Atlanta. 2010: 3978-3985.
[14] Wang JQ, Wang FX, Bao WB, Guan EL. Rotor Design and Strength Analysis of High Speed Permanent Magnet Machine. *Proceedings of the CSEE.* 2005; 25(15): 140 – 145.
[15] Binder A, Schneider T, Klohr M. Fixation of Buried and Surface-mounted Magnets in High-Speed Permanent-Magnet Synchronous Machines. *IEEE Transactions on Industry Applications*. 2006; 42(4): 1021–1037.
[16] Qian WC. Theoretical Basis of Motor Design and Strength Calculation. Hefei: Anhui Science & Techonology Publishing House.1992: 84-106. (In Chinese).